Journal of the Korean Electrochemical Society
Vol. 28, No. 4, 2025, 201-210
https://doi.org/10.5229/JKES.2025.28.4.201

Research Paper
pISSN 1229-1935
eISSN 2288-9000

산소발생반응 제고를 위한 Ag@Ir 코어-쉘 나노입자 전기촉매

홍승택[1] · Paula Marielle Ababao[1,2] · **오일환**[1]*

[1]금오공과대학교 응용화학과

[2]Mathematics and Physical Sciences Department, FEU Institute of Technology, Manila, 1015, Philippines

(2025년 8월 12일 접수 : 2025년 8월 18일 수정 : 2025년 9월 1일 채택)

Core-Shell Ag@Ir Nanoparticle Catalyst for Enhanced Oxygen Evolution Reaction

Seung-taek Hong[1], Paula Marielle Ababao[1,2], and Ilwhan Oh[1]*

[1]*Department of Applied Chemistry and Energy Convergence Engineering, Kumoh National Institute of Technology, Gumi, Gyeongbuk, South Korea*

[2]*Mathematics and Physical Sciences Department, FEU Institute of Technology, Manila, 1015, Philippines*

(Received October 31, 2025 : Revised November 24, 2025 : Accepted November 27, 2025)

초 록

산성 조건 하에서 산소 발생 반응(OER)에서 귀금속-귀금속 계면 결합의 역할을 밝히기 위해 화학적 환원법을 통해 Ag@Ir 코어-쉘 나노구조 촉매를 합성했다. XRF를 이용한 조성 최적화 결과, Ag@Ir(1:1)이 가장 활성이 높은 배열로 확인되었으며,질량 활성도는 6.39 A mg^{-1}, 과전압은 10 mA cm^{-2}에서 250 mV 였다(85% iR compensation). XPS 분석 결과, Ag와 Ir 사이의 약한 계면 전자 결합이 확인되어 Ir에서 Ag로의 전하 재분배가 나타났고, 두 성분의 금속성은 그대로 유지하면서 Ir^{3+}/Ir^{4+} 종이 풍부한 전자 결핍 Ir 표면이 형성되었다. 이러한 전자 상호작용은 Ir의 산화 상태를 미묘하게 조절하고 구조적 재구성 없이 OER 반응 속도를 촉진한다. 전기화학적 평가 결과, 12시간 작동 후 과전압이 약 30 mV 증가하는 등 안정적인 성능을 확인했다. 화학적으로 불활성인 Ag 코어는 계면의 온전성을 유지하고 제어된 전자 상호작용을 지원하여 균형 잡힌 활성과 내구성을 제공한다. 이러한 결과는 Ag@Ir 촉매가 Ir 기반 OER 촉매의 계면 전자 거동을 이해하기 위한 모델 귀금속-귀금속 시스템임을 보여준다.

Abstract : Ag@Ir core–shell nanostructured catalysts were synthesized through a chemical reduction method to investigate the role of noble–noble interfacial coupling in the oxygen evolution reaction (OER) under acidic conditions. Composition optimization by XRF identified Ag@Ir(1:1) as the most active configuration, achieving a mass activity of 6.39 A mg^{-1} and an overpotential of 250 mV at 10 mA cm^{-2} (85% iR compensation). XPS revealed weak interfacial electronic coupling between Ag and Ir, resulting in moderate charge redistribution from Ir to Ag and an electron-deficient Ir surface enriched in Ir^{3+}/Ir^{4+} species while preserving the metallic nature of both components. This electronic interaction subtly modulates Ir oxidation states and facilitates OER kinetics without structural reconstruction. Electrochemical testing confirmed steady performance with only a ~30 mV increase in overpotential after 12 h of operation. The chemically inert Ag core maintains interfacial integrity and supports controlled electronic inter-

*E-mail: ioh@kumoh.ac.kr

action, leading to balanced activity and durability. These results establish Ag@Ir as a model noble–noble system for understanding interfacial electronic behavior in Ir-based OER catalysts.

Keywords : hydrogen economy, water electrolysis, green hydrogen, oxygen evolution reaction, electrocatalysis

1. Introduction

The transition toward a green economy has intensified global efforts to reduce greenhouse gas emissions and achieve net-zero targets by 2050. Among clean energy carriers, hydrogen has emerged as an essential component for decarbonizing hard-to-abate sectors such as heavy industry, transportation, and power generation.[1–4] Green hydrogen, produced through water electrolysis using renewable electricity, offers a carbon-free alternative that supports large-scale renewable integration and long-term energy storage.[5–7] However, its widespread deployment remains limited by production costs, infrastructure needs, and the low efficiency of current electrolysis systems.[8–10]

In water electrolysis, the oxygen evolution reaction (OER) represents the rate-limiting step due to its sluggish four-electron transfer process and high overpotential.[11–13] Although noble-metal oxides such as IrO_2 and RuO_2 are the most efficient OER catalysts, their high cost, scarcity, and poor stability under acidic conditions hinder large-scale application.[14–18] Continuous oxidation and dissolution during operation lead to gradual performance decay, making the development of cost-effective and durable catalysts a key research priority.[19,20]

Efforts to improve OER performance have focused on modifying catalyst structure and electronic configuration through alloying, defect engineering, and surface design.[21–23] Among these approaches, core–shell and bimetallic nanostructures have shown promise in enhancing catalytic activity and reducing noble-metal consumption. These structures promote synergistic interactions between the core and shell, improving charge transfer, structural stability, and utilization of the active metal.[24–27]

In this context, Ag@Ir core–shell nanostructures offer an efficient strategy to improve OER performance while minimizing Ir usage. Silver, being highly conductive and relatively inexpensive, can act as an electron-rich core that supports a thin Ir shell, enhancing electronic coupling and stabilizing the active surface.[28,29] The interaction between Ag and Ir can modulate the Ir d-band center, facilitating adsorption and desorption of OER intermediates and lowering overpotential.[24,30]

This study reports the synthesis of Ag@Ir core–shell nanostructured catalysts through a facile chemical reduction process aimed at enhancing Ir utilization for the OER. The synthesis yielded a uniform Ir shell over a conductive Ag core, forming a well-defined interface that promotes efficient charge transfer and increases the accessibility of active Ir sites. Compared with commercial Ir nanoparticles, Ag@Ir catalyst demonstrated superior electrochemical performance with a reduced Ir content of 19.9 wt.%, achieving a mass activity of 6.39 A mg^{-1} at 1.55 V and an overpotential of 250 mV at 10 mA cm^{-2} (85% iR compensation). The optimized Ag@Ir core-shell catalyst demonstrates a cost-effective and durable alternative to conventional Ir-based catalysts, effectively addressing Ir scarcity while maintaining high activity and stability for sustainable hydrogen production.

2. Experimental Methods

2.1 Materials

Silver Nanoparticles (Ag, 99.99% 100 nm). Iridium (IV) chloride hydrate ($IrCl_4 \cdot xH_2O$, purity ≥ 99.8%), Sodium borohydride ($NaBH_4$, purity ≥ 98%), Nafion 117 solution (~5 wt.%) were purchased from Sigma-Aldrich. Ethanol solution (C_2H_5OH, purity ≥94.5%), Perchloric acid ($HClO_4$, purity ≥60%), and Mercury nitrate ($Hg(NO_3)_2 \cdot H_2O$, purity · 99.9%) were supplied by Daejung Chemicals and Metals (Siheung-si, South Korea).

2.2 Synthesis of Ag@Ir Nanoparticles

Ag@Ir core–shell nanoparticles were synthesized via a reduction-assisted chemical process. Initially,

77.5 mg of silver nanoparticles (Ag NPs) were ultrasonically dispersed in 80 mL of ethanol using a horn sonicator to obtain a stable colloidal suspension. The dispersion was then transferred to a two-neck round-bottom flask and heated to 70 °C under continuous stirring at 500 rpm using an overhead stirrer equipped with a Teflon paddle.

Separately, an iridium precursor solution was prepared by dispersing 40 mg of $IrCl_x \cdot H_2O$ in 50 mL of ethanol under identical sonication conditions. This precursor solution was slowly introduced into the Ag NP suspension to ensure uniform mixing. For the reduction step, sodium borohydride ($NaBH_4$) was dissolved in 20 mL of ethanol via bath sonication for 3 minutes, and the resulting reducing solution was injected into the reaction flask at a controlled flow rate of 3.33 mL min^{-1}. Throughout the reduction, the temperature and stirring speed were maintained at 70 °C and 500 rpm, respectively. After the complete addition of $NaBH_4$, the reaction was allowed to proceed for an additional 2 hours to ensure complete shell formation.

Upon completion, the mixture was cooled to room temperature (~25 °C) by immersing the flask in an ice bath for 15 minutes. The resulting suspension was transferred into 50 mL centrifuge tubes and subjected to sequential washing to remove unreacted precursors and by-products. The product was washed twice with ethanol by centrifugation at 10,000 rpm for 10 minutes each, followed by a final wash with deionized water at 13,000 rpm for 15 minutes.

To recover the solid product, the washed sample was first dried in a vacuum oven at 35 °C for 8 hours to remove residual solvents, then further dried at 90 °C for 12 hours to yield the final Ag@Ir core–shell catalyst powder.

2.3 Preparation of Catalyst Ink

Catalyst ink was prepared at a concentration of 0.2 mg mL^{-1} for electrochemical evaluation. In a typical procedure, 1 mg of Ag@Ir core–shell nanoparticles was dispersed in a mixed solvent containing 1.5 mL of deionized water, 0.5 mL of isopropyl alcohol, and 20 μL of Nafion 117 solution as a binding agent. The mixture was sonicated for 3 minutes in a bath sonicator to achieve a homogeneous and stable suspension.

For electrode fabrication, 10 μL of the catalyst ink was drop-cast onto the surface of a 3 mm rotating disk electrode (RDE) and air-dried under ambient conditions prior to electrochemical measurements. This procedure ensured uniform catalyst loading and good adhesion of the catalyst film to the electrode surface.

2.4 Physicochemical Characterization

The physicochemical characteristics of the synthesized Ag@Ir core–shell nanoparticles were comprehensively examined using advanced analytical techniques. The morphology, lattice structure, and elemental distribution were characterized by spherical aberration–corrected scanning transmission electron microscopy (CS-STEM, JEOL JEM-ARM200F) equipped with a dual-detector energy-dispersive X-ray spectroscopy (EDS) system. High-resolution STEM images were used to measure the lattice fringe spacing (d-spacing) values quantitatively through ImageJ software. The crystalline structure of the samples was analyzed using X-ray diffraction (XRD) with Cu Kα radiation (λ = 1.5406 Å) operated at 40 kV and 30 mA. Diffraction patterns were collected over a 2θ range of 20°–100°, employing a scan rate of 2° min^{-1} and a step size of 0.02°, to identify crystalline phases and confirm the formation of the Ag@Ir core–shell architecture.

The surface chemical composition and oxidation states of the constituent elements were investigated through X-ray photoelectron spectroscopy (XPS, PHI 5000 VersaProbe III) using a monochromatic Al Kα X-ray source (1486.6 eV, 25.2 W). The chamber pressure during measurement was maintained below 1×10^{-9} Torr. A wide-range survey spectrum (0–1200 eV) was first recorded to determine the elemental composition, followed by high-resolution scans in the Ag 3d, Ir 4f, and C 1s regions. The spectra were collected with a pass energy of 26 eV and an energy step size of 0.1 eV. All binding energies were calibrated relative to the C 1s reference peak at 284.8 eV. Background subtraction was performed using the Shirley method, and peak deconvolution and quantification were conducted with CasaXPS software to ensure accurate chemical state analysis.

2.5 Electrochemical Characterization

Electrochemical measurements were carried out using a Bio-Logic SP-150 potentiostat in a conventional three-electrode configuration. A gold rotating disk electrode (Au RDE, 3 mm in diameter; geometric area = 0.071 cm^2) coated with the catalyst ink served as the working electrode. A platinum mesh and a saturated calomel electrode (SCE) were employed as the counter and reference electrodes, respectively. All tests were performed in 0.1 M $HClO_4$ aqueous electrolyte at room temperature (~25 °C). Before each experiment, the electrolyte was purged with high-purity N_2 for at least 30 minutes to ensure N_2-saturated conditions. All measured potentials were converted to the reversible hydrogen electrode (RHE) scale, with the pH of 0.1 M $HClO_4$ approximately equal to 1.0.

The OER activity was evaluated using linear sweep voltammetry (LSV) at a scan rate of 10 mV s^{-1} and a rotation speed of 2500 rpm. Tafel slopes were extracted from the LSV polarization curves. Long-term operational stability was assessed via chronopotentiometry at a constant current density of 10 mA cm^{-2} for 12 h. An 85% iR-compensation was applied to all electrochemical data. Mass activity was normalized to the active Ir mass, defined as the mass of Ir deposited on the RDE's geometric surface area of 0.071 cm^2 and calculated by multiplying the catalyst loading by the Ir wt% obtained from XRF.

The electrochemically active surface area (ECSA) was determined using mercury underpotential deposition (Hg UPD) in 1.0 M $HClO_4$ containing 1 mM $Hg(NO_3)_2$. Cyclic voltammograms were recorded in the potential range of 0.5–0.9 V vs RHE at scan rates between 10 and 40 mV s^{-1}, and the ECSA was calculated from the integrated charge associated with the Hg desorption peak. The turnover frequency (TOF) was calculated from the current density at 1.55 V vs RHE, normalized by the number of electrochemically active Ir sites determined from the ECSA. All electrochemical data were processed and analyzed using EC-Lab software (Bio-Logic). Each experiment was repeated multiple times to ensure reproducibility and accuracy of the measurements.

3. Results and Discussion

Catalyst optimization was performed by varying the Ir–Ag mass ratio to identify the composition that provides the highest catalytic efficiency while minimizing Ir consumption. Fig. 1a presents the mass activity as a function of the Ir–Ag ratio, together with the corresponding Ir wt.% content obtained from XRF measurements. Among all samples, the Ag@Ir(1:1) composition exhibited the highest mass activity of 6.39 A mg^{-1}, surpassing both Ir-rich and Ag-rich counterparts. This optimum balance arises from sufficient Ir surface coverage

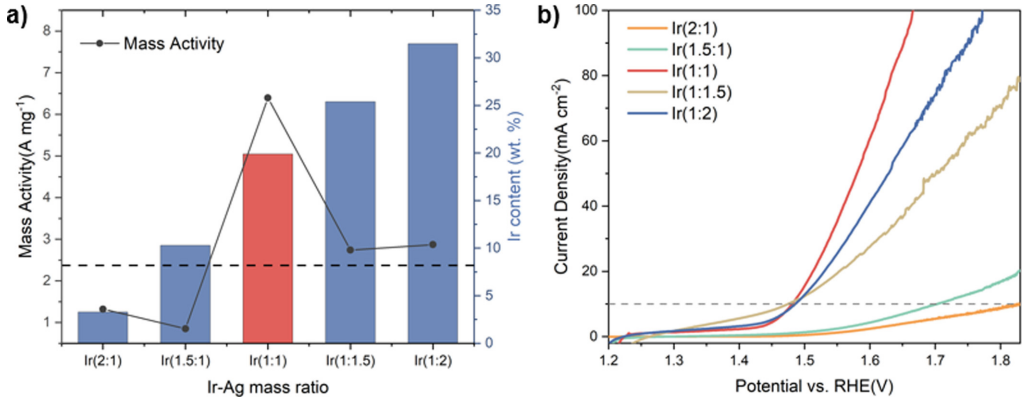

Fig. 1. (a) Mass activity of Ag@Ir catalysts prepared with varying Ag:Ir mass ratios, alongside the corresponding Ir contents determined by XRF. The broken horizontal line indicates the mass activity benchmark of Ir black. (b) Linear sweep voltammetry (LSV) profiles of Ag@Ir catalysts recorded in 0.1 M $HClO_4$ at a scan rate of 10 mV s^{-1}. The broken horizontal line denotes the reference current density of 10 mA cm^{-2}.

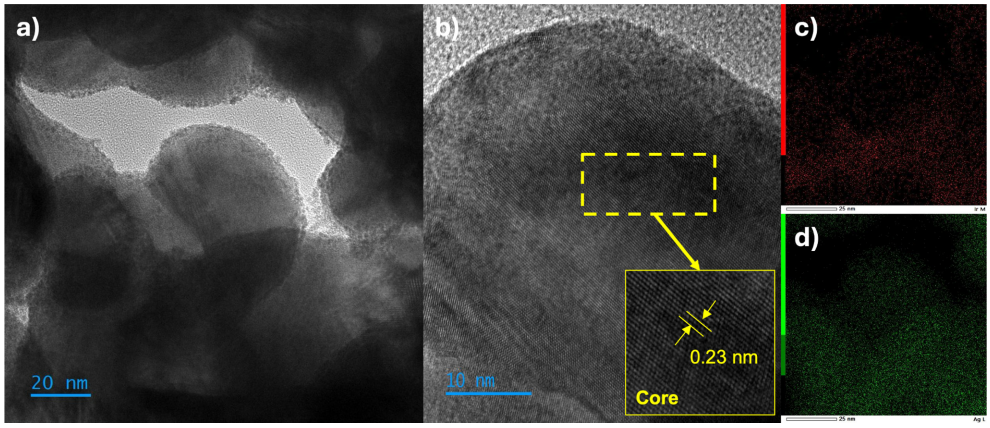

Fig. 2. TEM and STEM-EDS mapping images of Ag@Ir core-shell nanostructures. a) Low-magnification(20nm) TEM image. b) High-resolution TEM(HRTEM) image showing the core-shell structure with a lattice spacing of 0.23nm corresponding to the Ag(111) plane. c) Ir elemental mapping(red), and d) Ag elemental mapping(green).

that maximizes the number of active sites while maintaining good electron transport through the Ag core. As shown in Fig. 1b, the polarization curves confirm that Ag@Ir(1:1) delivers the highest current density across the entire potential range, indicating superior intrinsic activity. At lower Ir content, catalytic performance decreases due to an insufficient number of Ir active sites, whereas excessive Ir loading hinders charge transport and increases particle agglomeration. Therefore, the Ag@Ir(1:1) catalyst achieves the most efficient utilization of Ir and was subsequently selected for further physicochemical and electrochemical characterization.

TEM and EDS analyses (Fig. 2a–d) confirm the successful formation of Ag@Ir core–shell nanostructures synthesized via chemical reduction. The TEM images reveal a distinct contrast between the dense Ag core and the surrounding Ir shell, verifying a well-defined core–shell architecture. The measured lattice spacing of 0.23 ± 0.01 nm corresponds to the (111) plane of face-centered cubic (fcc) Ag, consistent with the reference value. The EDS elemental mapping further confirms the homogeneous distribution of Ir around the Ag core, with no visible aggregation or phase segregation.

XRD analysis (Fig. 3) shows distinct reflections at 2θ = 38.1°, 44.3°, 64.4°, 77.4°, and 81.5°, corresponding to the (111), (200), (220), (311), and (222) planes of fcc Ag. No diffraction peaks attributable to crystalline Ir are detected, indicating that

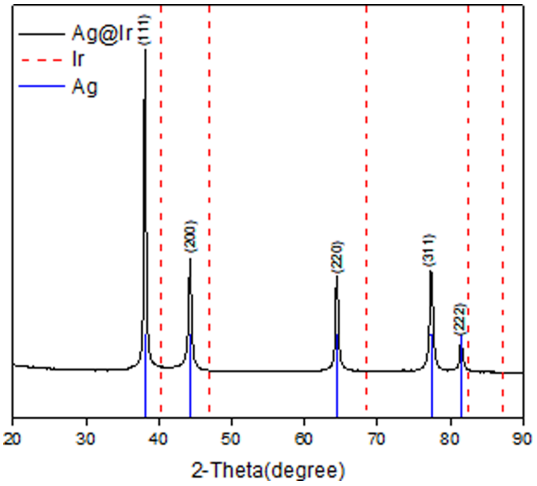

Fig. 3. XRD pattern of Ag@Ir(1:1) recorded using Cu Kα radiation (λ = 1.5406 Å), showing diffraction peaks corresponding to the (111), (200), (220), (311), and (222) planes of fcc Ag. Reference peak positions for Ag and Ir are included for comparison.

the Ir shell is predominantly amorphous or ultrathin, consistent with its nanoscale thickness being below the detection limit of XRD. The absence of peak shifts relative to pure Ag confirms that Ir deposition does not perturb the Ag lattice, in contrast to systems such as Ir/Au nanoclusters where lattice compression induces measurable 2θ shifts. These results collectively show that Ir forms a conformal, non-alloyed coating on the Ag core, preserving

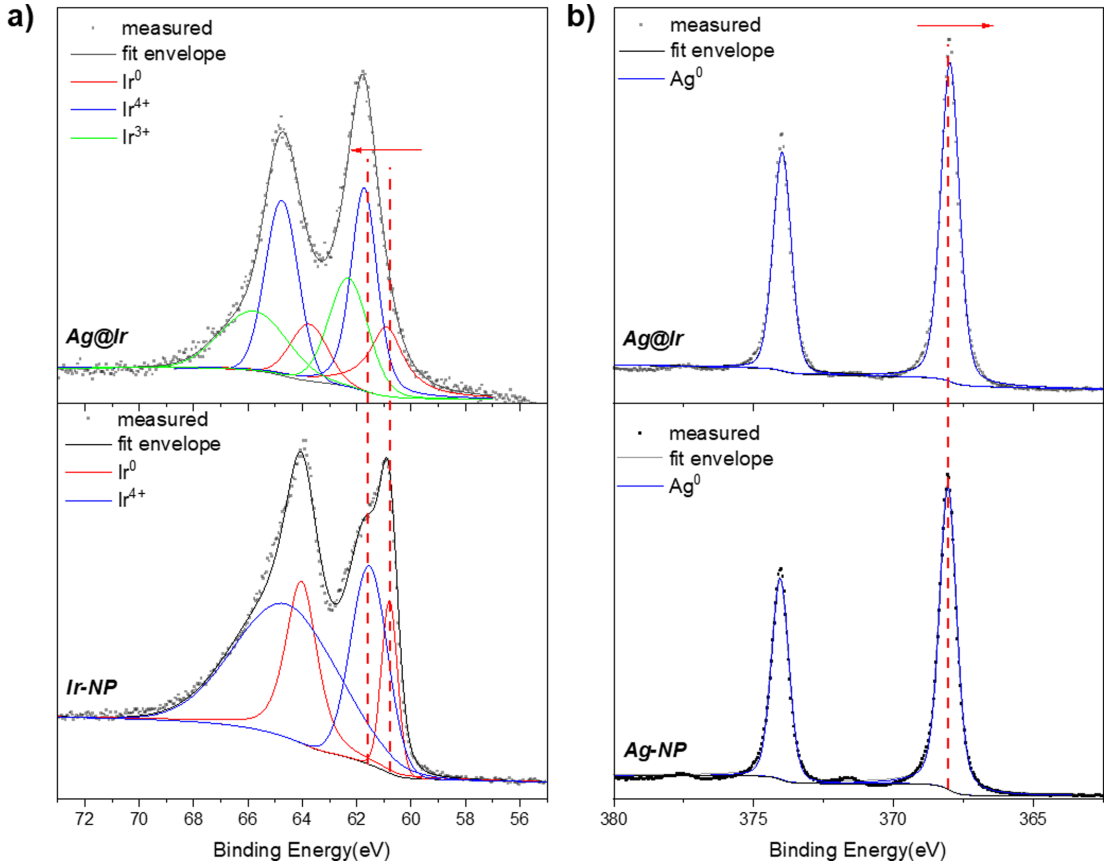

Fig. 4. (a) XPS spectra of Ir 4f region for Ag@Ir and Ir-NP showing deconvoluted peaks corresponding to Ir^0, Ir^{3+}, and Ir^{4+} species. (b) XPS spectra of Ag 3d region for Ag@Ir and Ag-NP indicating the binding energies of metallic Ag^0.

the structural integrity of Ag while providing an amorphous Ir surface rich in unsaturated coordination sites that are favorable for OER catalysis.

XPS characterization was performed to evaluate the surface composition and interfacial electronic state of Ag@Ir. The spectra were calibrated to the C 1s line at 284.8 eV and fitted using Gaussian–Lorentzian functions. In the Ir 4f region (Fig. 4a), three chemical states corresponding to Ir^0, Ir^{3+}, and Ir^{4+} were identified. The Ir^{4+} $4f_{7/2}$ peak shifted from 61.54 to 61.74 eV (+0.20 eV) and Ir^0 from 60.81 to 60.93 eV (+0.12 eV), while a minor Ir^{3+} signal appeared at 62.34 eV. These small positive shifts suggest limited electron depletion from Ir, indicating weak but measurable charge migration from the Ir shell toward the Ag core.

The Ag 3d spectrum (Fig. 4b) displayed a corresponding negative shift of the Ag^0 $3d_{5/2}$ peak from 368.04 to 367.98 eV (−0.06 eV), confirming mild electron accumulation in Ag. The coexistence of Ir^0/Ir^{3+}/Ir^{4+} species implies that Ir maintains a partially metallic character, while the absence of Ag oxide features confirms that the Ag core remains chemically inert. This combination evidences weak interfacial electronic coupling between the Ag core and Ir shell, in which moderate charge redistribution occurs without inducing chemical reactivity or structural modification.

Unlike transition-metal–supported Ir catalysts, where strong electron transfer accompanies core oxidation or dissolution, the Ag–Ir interface remains electronically stable and chemically preserved. This behavior contrasts with the pronounced Ir→Ni charge transfer observed in transition-metal cores[24)]

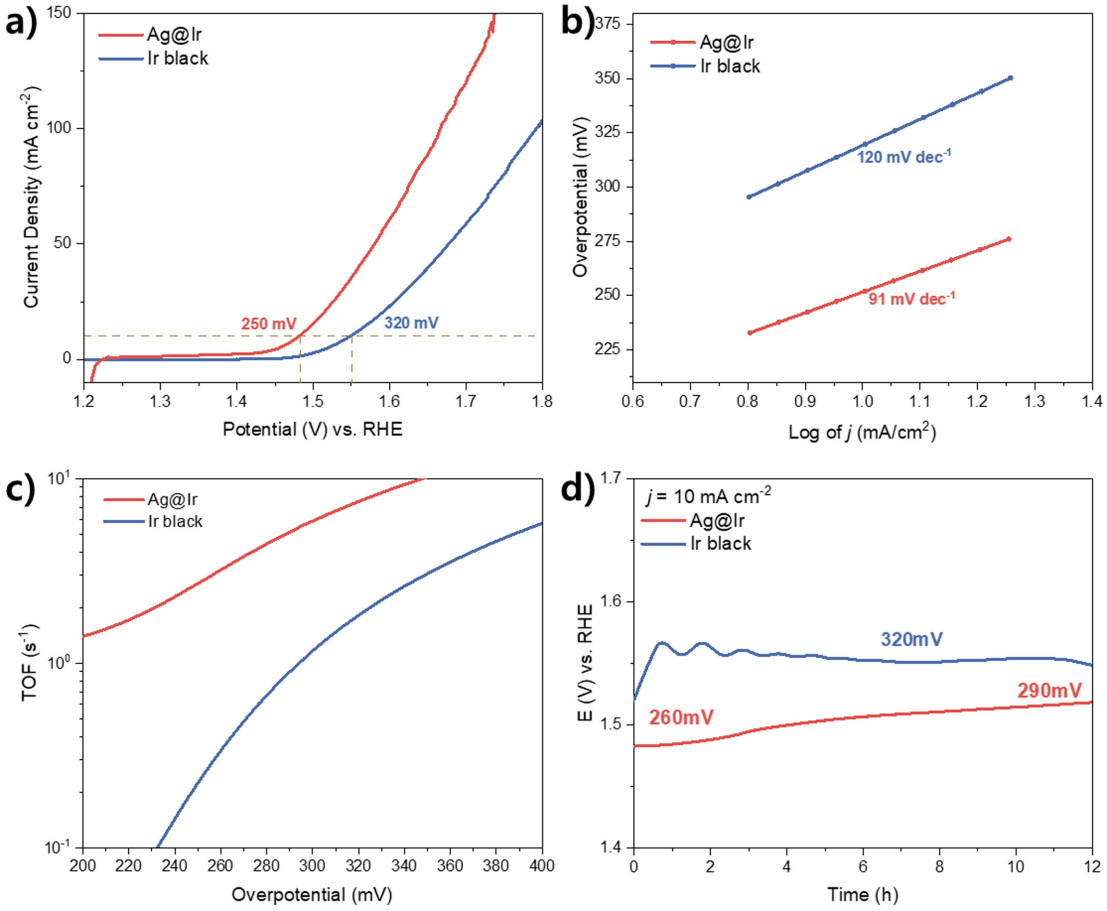

Fig. 5. (a) iR-corrected (85%) LSV curves of Ag@Ir(1:1) and Ir black in 0.1 M $HClO_4$ at a scan rate of 10 mV s^{-1}. (b) Tafel plots derived from polarization data. (c) TOF plots of Ag@Ir(1:1) and Ir black. (d) Chronoamperometric stability test of Ag@Ir(1:1) and Ir black recorded at a constant current density of 10 mA cm^{-2} for 12 h.

and the opposite Au→Ir donation reported for Ir/Au nanoclusters.[31] The Ag@Ir system therefore represents an intermediate coupling regime, combining the chemical stability characteristic of noble–noble junctions with sufficient electronic interaction to modulate Ir oxidation states that are favorable for OER catalysis.

The influence of passive electronic coupling on the electrocatalytic behavior of Ag@Ir was evaluated under acidic conditions (0.1 M $HClO_4$). Linear sweep voltammetry (LSV) measurements (Fig. 5a) reveal that Ag@Ir(1:1) requires an overpotential of 250 mV to achieve a current density of 10 mA cm^{-2} (85% compensation applied), which is lower than 320 mV for commercial Ir black. This reduction in overpotential, though moderate, demonstrates that even weak Ir→Ag charge redistribution is sufficient to modify surface electronic states and enhance OER activity. The presence of mixed Ir^{3+}/Ir^{4+} species, as identified by XPS, provides the necessary redox flexibility for oxygen intermediate formation while preserving the metallic continuity of the Ir shell.

The corresponding Tafel plots (Fig. 5b) exhibit slopes of 91 mV dec^{-1} for Ag@Ir and 120 mV dec^{-1} for Ir black, indicating more favorable reaction kinetics on the Ag@Ir surface. This improvement aligns with the weak Ir→Ag charge redistribution observed by XPS, where slight electron depletion from Ir stabilizes mixed Ir^{3+}/Ir^{4+}

states known to promote OER intermediate formation. The modulation of Ir surface oxidation states provides more redox-flexible active sites, contributing to the lower Tafel slope and enhanced kinetic response. In addition, the conductive Ag core supports efficient electron transport, while the partially oxidized Ir shell facilitates the adsorption–desorption steps of the OER. This combined effect produces a stable yet active configuration in which the Ag core remains inert and the Ir shell maintains its catalytic identity without undergoing irreversible oxidation.

Intrinsic catalytic activity, evaluated through mass activity and turnover frequency (TOF), further supports this interpretation. Ag@Ir(1:1) achieves a mass activity of 6.39 A mg^{-1} at 1.55 V vs. RHE, exceeding that of Ir black. Moreover, as shown in Fig. 5c, Ag@Ir(1:1) exhibits TOF values up to approximately one order of magnitude higher than Ir black at comparable overpotentials (e.g., ~320 mV, where Ir black reaches its reference overpotential). This pronounced TOF enhancement indicates that each accessible Ir site on Ag@Ir(1:1) turns over OER more frequently, reflecting more efficient Ir utilization despite the reduced overall Ir loading.

Unlike transition-metal–supported systems, where aggressive charge transfer often leads to oxidation of the core and subsequent degradation[24], the Ag–Ir interface maintains a delicate balance between electronic interaction and chemical stability. The inert nature of Ag prevents oxide formation or dissolution, allowing Ir to operate within an electronically tuned but structurally preserved environment. Consequently, Ag@Ir demonstrates consistent OER performance without the instability typically associated with reactive cores such as Ni or Co.

The electrochemical results therefore validate the effect of noble–noble interfacial coupling predicted from XPS analysis. The Ag–Ir interaction produces a mildly electron-deficient Ir shell that remains catalytically active yet structurally stable during operation. This balance of moderate enhancement and interfacial resilience defines a distinct catalytic regime, one governed not by extensive electronic reconstruction, but by self-limiting charge redistribution and inert interfacial coupling.

Chronopotentiometric testing (Fig. 5d) demonstrates that Ag@Ir maintains stable OER operation at 10 mA cm^{-2}, with the overpotential increasing modestly from 260 mV to 290 mV over 12 h. The small drift of ~30 mV (2.5 mV h^{-1}) reflects ~89% retention of the initial potential, indicating only gradual performance decay under continuous anodic polarization. By contrast, commercial Ir black begins at a higher overpotential (~320 mV) and exhibits larger fluctuations over the same duration, underscoring its inferior operational robustness.

The mild performance decay observed for Ag@Ir is most plausibly associated with surface processes on the Ir shell, rather than degradation of the Ag core. XPS and XRD analyses acquired prior to OER operation show no evidence of Ag oxidation or lattice distortion, consistent with the chemical inertness of Ag in acidic anodic environments. While post-OER dissolution analysis was not available in this study, the absence of Ag-based signatures in the initial state and the known stability of Ag under these conditions suggest that the core is unlikely to be the dominant contributor to degradation.

Instead, the moderate rise in potential is consistent with gradual Ir surface oxidation, hydroxide layer restructuring, or partial loss of active Ir sites, processes compatible with the mixed Ir^{3+}/Ir^{4+} states identified by XPS and with the shell-localized redox activity expected for core–shell noble-metal catalysts. The Ag core continues to provide a mechanically and electronically stable support, while the Ir shell retains its catalytic function with only minor surface evolution during extended operation.

4. Conclusion

This study demonstrates the effective development of Ag@Ir core–shell nanostructures as highly active and durable OER catalysts in acidic media. Systematic variation of the Ag–Ir mass ratio identified Ag@Ir(1:1) as the optimal configuration, delivering the highest mass activity and the lowest overpotential among the tested compositions. Structural characterization confirmed a crystalline Ag core coated by an amorphous Ir shell, while XPS revealed a weak Ir→Ag charge redistribution that stabilizes mixed Ir^{3+}/Ir^{4+} surface states known to facilitate

OER intermediates. These electronically modulated Ir sites, together with the conductive Ag support, contribute to enhanced charge-transfer kinetics and superior activity relative to commercial Ir black.

Ag@Ir(1:1) also exhibited strong operational stability, with only a ~30 mV increase in overpotential over 12 h of continuous chronopotentiometric operation. Pre-OER XPS and XRD data indicate that the Ag core remains chemically inert, suggesting that the mild degradation observed is primarily associated with surface evolution of the Ir shell rather than core deterioration. These findings highlight the ability of the Ag core–Ir shell configuration to preserve catalytic functionality while minimizing Ir usage. Overall, the Ag@Ir architecture provides a balanced combination of high activity, efficient Ir utilization, and sustained stability in acidic OER, offering a promising and cost-effective pathway for advancing PEM water-electrolysis catalyst design.

Acknowledgement

This research was supported by Kumoh National Institute of Technology (2024–2026) and the Gyeongsangbuk-do RISE (Regional Innovation System & Education) project (Specialized Industry Scale-up unit).

References

1. F. M. Mohsen, H. M. Mjbel, A. F. Challoob, R. Alkhazaleh, and A. Alahmer, Advancements in green hydrogen production: A comprehensive review of prospects, challenges, and innovations in electrolyzer technologies, *Fuel*, **404(Part B)**, 136251 (2026).
2. S. Algburi, O. Al-Dulaimi, H. F. Fakhruldeen, D. H. Khalaf, R. N. Hanoon, F. I. Jabbar, Q. Hassan, A. K. Al-Jiboory, and S. Kiconco, The green hydrogen role in the global energy transformations, *Renew. Sustain. Energy Transit.*, **8**, 100118 (2025).
3. D. Belkhiri, M. Ajaamoum, F. Outferdine, A. El Idrissi, and E. Boulaoutaq, Hotspots in hydrogen research and developments: Current status, pathways, challenges, and vision to 2050, *e-Prime – Adv. Electr. Eng., Electron. Energy*, **13**, 101089 (2025).
4. A.-M. Chirosca, E. Rusu, and V. Minzu, Green hydrogen—production and storage methods: current status and future directions, *Energies*, **17(23)**, 5820 (2024).
5. B. A. C. Roque, M. H. C. Cavalcanti, P. P. F. Brasileiro, P. H. R. P. Gama, V. A. dos Santos, A. Converti, M. Benachour, and L. A. Sarubbo, Hydrogen-powered future: catalyzing energy transition, industry decarbonization and sustainable economic development: a review, *Gondwana Res.*, **140**, 159–180 (2025).
6. P. Kumar and H. K. Channi, Hydrogen energy: a new era of clean energy toward sustainable development, in *Challenges and Opportunities in Green Hydrogen Production*, P. Singh, A. K. Agarwal, A. Thakur, and R. K. Sinha, Eds., pp. 55–82, Springer, Singapore (2024).
7. A. O. M. Maka, M. Mehmood, and T. N. Chaudhary, Green hydrogen revolution and its pathway towards sustainable development, *Clean Energy*, **9(2)**, 124–131 (2025).
8. Z. Sun, Hydrogen energy: development prospects, current obstacles and policy suggestions under China's "dual carbon" goals, *Chin. J. Urban Environ. Stud.*, **11(1)**., 2350006 (2023).
9. P. Sachdeva and A. K. Chaudhry, Hydrogen: empowering sustainable transportation and mitigating greenhouse gas emissions, in *Renewable Hydrogen*, M. Bibra, R. K. Sani, and S. Kumar, Eds., pp. 137–150, Elsevier, 2024.
10. E. L. Carlson, K. Pickford, and H. Nyga-Łukaszewska, Green hydrogen and an evolving concept of energy security: challenges and comparisons, *Renew. Energy*, **219(1)**, 119410 (2023).
11. X. Liu, Z. He, M. Ajmal, *et al.*, Recent advances in the comprehension and regulation of lattice oxygen oxidation mechanism in oxygen evolution reaction, *Trans. Tianjin Univ.*, **29**, 247–253 (2023).
12. L. Chen, Y. Liu, H. Cong, Q. Ge, W. Zhao, N. Jiang, and Q. Zhang, Recent progress and perspective for oxygen evolution reaction under acidic environments, *Mater. Chem. Front.*, **8(4)**., 986-1014 (2024).
13. G. Gao, Z. Sun, X. Chen, G. Zhu, B. Sun, Y. Yamauchi, and S. Liu, Recent advances in Ru/Ir-based electrocatalysts for acidic oxygen evolution reaction, *Appl. Catal. B: Environ.*, **343**, 123584 (2024).
14. H. Dehghan-Manshadi, M. Mazloum-Ardakani, and S. Ghayempour, Dual-atom catalysts for oxygen evolution reaction, in *Atomically Precise Electrocatalysts for Electrochemical Energy Applications*, A. Kumar and R. K. Gupta, Eds., pp. 203–217, Springer, Cham (2024).
15. T. Liu, C. Chen, Z. Pu, Q. Huang, X. Zhang, A. M. Al-Enizi, A. Nafady, S. Huang, D. Chen, and S. Mu, Non-noble-metal-based electrocatalysts for acidic oxygen evolution reaction: recent progress, challenges, and perspectives, *Small*, **20**, 2405399 (2024).
16. M. Carmo, D. L. Fritz, J. Mergel, and D. Stolten, A comprehensive review on PEM water electrolysis, *Int. J. Hydrogen Energy*, **38(12)**, 4901–4934 (2013).
17. A. Qadir, Z. Haider, U. Farooq, S. Shafique, S. Karim, H. Xu, and S. Ahmed, Advancements in acidic OER and HER electrocatalysts: Iridium, MOF-based, and ruthenium systems for sustainable hydrogen production, *Int. J. Hydrogen Energy*, 152, 150188 (2025).

18. P. M. Ababao and I. Oh, Recent advances in catalyst materials for PEM water electrolysis, *J. Korean Electrochem. Soc.*, **26(2)**, 19–34 (2023).
19. I. M. S. Anekwe and Y. M. Isa, Unlocking catalytic longevity: a critical review of catalyst deactivation pathways and regeneration technologies, *Energy Adv.*, **4(9)**, 1075–1113 (2025).
20. Y. Xie, F. Luo, and Z. Yang, Strategies for the enhancements in catalytic performance and stability of anodic electrocatalyst in PEM water splitting, *Energy Rev.*, **3(4)**, 100103 (2024).
21. M. Singh, D. R. Paudel, H. Kim, T. H. Kim, J. Park, and S. Lee, Interface engineering strategies for enhanced electrocatalytic hydrogen evolution reaction, *Energy Adv.*, **4(6)**, 716–742 (2025).
22. Q. Kang, D. Lai, W. Tang, Q. Lu, and F. Gao, Intrinsic activity modulation and structural design of NiFe alloy catalysts for an efficient oxygen evolution reaction, *Chem. Sci.*, **12(11)**, 3818–3835 (2021).
23. G. Sheng, S. Zhao, U. Naeem, F. N. A. Saad, R. Lyu, X. Jiang, S. Hu, S. Kheawhom, R. Yin, H. Song, A. Alshoaibi, W. Shao, and A. A. Mohamad, Rational design of transition metal-based heterostructure electrocatalysts for high-performance oxygen evolution reaction, *Int. J. Hydrogen Energy*, **127**, 717–736 (2025).
24. P. M. Ababao, J. J. Bofill, and I. Oh, Mass activity boost in Ni@Ir nanowire catalysts for oxygen evolution reaction in PEM water electrolysis, *Int. J. Hydrogen Energy*, **118**, 441–448 (2025).
25. M. Yasutake, Z. Noda, J. Matsuda, S. M. Lyth, M. Nishihara, K. Ito, A. Hayashi, and K. Sasaki, Ru-core Ir-shell electrocatalysts deposited on a surface-modified Ti-based porous transport layer for polymer electrolyte membrane water electrolysis, *Int. J. Hydrogen Energy*, **49(C)**, 169–183 (2024).
26. Y. Xu, C. Wang, T. Du, C. Yang, and X. Zhu, Mo-doped IrCo@Ir core–shell catalysts enhanced performance and stability in the oxygen evolution reaction of PEM water electrolysis, *Appl. Surf. Sci.*, **714**, 164445 (2025).
27. J. Hyun and C. Pak, Facile preparation of core–shell Ru@Ir/C catalyst as a bifunctional electrocatalyst for reversal-tolerant anode in polymer electrolyte membrane fuel cell, *J. Power Sources*, **626**, 235716 (2025).
28. A. Saad, D. Liu, Y. Wu, Z. Song, Y. Li, T. Najam, K. Zong, P. Tsiakaras, and X. Cai, Ag nanoparticles modified crumpled borophene supported Co_3O_4 catalyst showing superior oxygen evolution reaction (OER) performance, *Appl. Catal. B: Environ.*, **298**, 120529 (2021).
29. Y. Zhou, S. Cheng, S. Lin, H. Du, J. Meng, and H. Qin, Construction and electrocatalytic performance of lignin-based Ag/FC catalysts, *Int. J. Electrochem. Sci.*, **19(1)**, 100455 (2024).
30. Y. Xie, C. Chang, F. Luo, and Z. Yang, Modulation in the d band of Ir by core–shell construction for robust water splitting electrocatalysts in acid, *ACS Appl. Mater. Interfaces*, **15(16)**, 20081–20088 (2023).
31. J. J. Bofill, P. M. Ababao, J. Lee, S. Hong, and I. Oh, Optimization of Ir/Au nanoclusters as electrocatalyst for oxygen evolution reaction in water electrolysis, *J. Korean Electrochem. Soc.*, **27(4),** 169–176 (2024).